Title

Dissipation and energy propagation across scales in an active cytoskeletal material

Journal

Proceedings of the National Academy of Sciences of the United States of America, 120(14)

ISSN

0027-8424

Authors

Foster, Peter J
Bae, Jinhye
Lemma, Bezia
et al.

Publication Date

2023-04-04

DOI

10.1073/pnas.2207662120

Peer reviewed

PNAS RESEARCH ARTICLE | PHYSICS

Dissipation and energy propagation across scales in an active cytoskeletal material

Peter J. Foster[a,b,1,2,3], Jinhye Bae[c,d,1], Bezia Lemma[b,e,f], Juanjuan Zheng[c], William Ireland[c], Pooja Chandrakar[b,f], Rémi Boros[f], Zvonimir Dogic[b,f], Daniel J. Needleman[c,g,h], and Joost J. Vlassak[c,3]

Edited by Christopher Jarzynski, University of Maryland, College Park, MD; received May 9, 2022; accepted February 22, 2023

Living systems are intrinsically nonequilibrium: They use metabolically derived chemical energy to power their emergent dynamics and self-organization. A crucial driver of these dynamics is the cellular cytoskeleton, a defining example of an active material where the energy injected by molecular motors cascades across length scales, allowing the material to break the constraints of thermodynamic equilibrium and display emergent nonequilibrium dynamics only possible due to the constant influx of energy. Notwithstanding recent experimental advances in the use of local probes to quantify entropy production and the breaking of detailed balance, little is known about the energetics of active materials or how energy propagates from the molecular to emergent length scales. Here, we use a recently developed picowatt calorimeter to experimentally measure the energetics of an active microtubule gel that displays emergent large-scale flows. We find that only approximately one-billionth of the system's total energy consumption contributes to these emergent flows. We develop a chemical kinetics model that quantitatively captures how the system's total thermal dissipation varies with ATP and microtubule concentrations but that breaks down at high motor concentration, signaling an interference between motors. Finally, we estimate how energy losses accumulate across scales. Taken together, these results highlight energetic efficiency as a key consideration for the engineering of active materials and are a powerful step toward developing a nonequilibrium thermodynamics of living systems.

active matter | molecular motors | picocalorimeter | energetic efficiency

Significance

While the flow of energy allows active materials to display rich emergent phenomena, such as self-organized flows, how much energy active materials use and how this energy propagates across length scales are not well understood. Here, we use picocalorimetry to measure the heat production rate of a microtubule active gel. By comparing the total rate of energy consumption (measured using calorimetry) with the rate of energy dissipation by the emergent flows (estimated from microscopy), we find that the energetic efficiency of this material is surprisingly low: Only approximately one-billionth of the system's total energy consumption propagates to the scale of the emergent flows. These results highlight energetic efficiency as a key material property for the engineering of active materials.

Energy Transduction across Length Scales

Active cytoskeletal materials display a broad range of nonequilibrium dynamics that are only possible due to the injection of energy at the microscale (1–9). We study the energetics of a well-characterized active material by leveraging a recently developed micromachined picocalorimeter sensor (10) to directly measure the total thermal dissipation of this material in its nonequilibrium steady state (Fig. 1 *A* and *B* and *Materials and Methods*). This instrument is particularly well suited for probing the energetics of biologically active materials due to its ability to measure the thermal dissipation of small, microliter-sized liquid samples with extraordinary sensitivity and a resolution of ~200 pW. In this instrument, differing heat production by a sample and a reference leads to a temperature differential across a thermopile, which in turn creates a voltage difference proportional to the thermally dissipated power due to the Seebeck effect (Fig. 1*B*) (11).

Microtubule active gels driven by kinesin motor clusters are a powerful model system for probing the energetics of active materials as they contain a minimal number of components and display nonequilibrium steady-state flows (6–8, 12, 13) (Fig. 1*C* and *Materials and Methods*). At the microscale, clusters of kinesin motors cross-link pairs of microtubules and use energy from the hydrolysis of ATP into ADP and P_i to drive their relative motion (Fig. 1*D*). Here, motor clusters are made of K401, an engineered form of *Drosophila* kinesin-1 truncated to the first 401 amino acids of the N-terminal. Through an inverse energy cascade, the energy from this protein-scale ATP hydrolysis is propagated across scales to the dynamics of mesoscale microtubule bundles. These microtubule bundles generate and are advected by autonomous flows that persist for hours on length scales far greater than the average length of microtubules, which are approximately 1 μm long (14) (Fig. 1*E* and Movie S1). To sustain steady-state dynamics, the system contains a pyruvate kinase(PK)–based ATP regeneration system, which catalyzes the conversion of ADP and phosphoenolpyruvate (PEP) to ATP and pyruvate. We placed 0.5 μL droplets of microtubule-based active gel under oil, a configuration compatible with either calorimetry (Fig. 1*A*) or microscopy measurements (Fig. 1*C*). To quantify the properties of these emergent large-scale flows, we measured the velocity field of the microtubule network using particle imaging velocimetry (PIV)

Competing interest statement: The authors have patent filings to disclose, the sensor used to perform the calorimetric measurements is currently under patent filing (US20190383758A1). Patent applicants: President and Fellows of Harvard College; Inventors: J.B. and J.J.V.

This article is a PNAS Direct Submission.

[1]P.J.F. and J.B. contributed equally to this work.

[2]Present address: Department of Physics and Astronomy, Bridge Institute, Michelson Center for Convergent Bioscience, University of Southern California, Los Angeles, CA 90089.

[3]To whom correspondence may be addressed. Email: peterfos@usc.edu or vlassak@seas.harvard.edu.

This article contains supporting information online at https://www.pnas.org/lookup/suppl/doi:10.1073/pnas.2207662120/-/DCSupplemental.

Published March 31, 2023.

(Fig. 1*E* and *Materials and Methods*) and extracted the mean flow speed, $\langle |\vec{v}(\vec{r},t)| \rangle_{\vec{r},t} = 2.9 \pm 1.1 \frac{\mu m}{s}$, and the spatial velocity autocorrelation $\langle \vec{v}(\vec{r},t) \cdot \vec{v}(\vec{r}+\vec{R},t) \rangle_t$ which decayed over a characteristic correlation length, $L = 135 \pm 44$ μm (*Materials and Methods*). Both the mean speed and the correlation length rapidly reach steady-state values similar to previous bulk fluid flow measurements in this system (13), arguing that the characterized flow properties represent bulk properties and that the oil–fluid interface does not significantly impact the emergent flows (Fig. 1*F*).

We first quantified the total power dissipated by the system using calorimetry and find that over the course of a ≈7-min measurement scan, the thermal dissipation of the active gels remains relatively constant (Fig. 1*G*). While data were collected for each sample at discrete intervals for over an hour (*SI Appendix*, Fig. S2), we here focus on measurements collected during the first scan to minimize potential confounding effects from thermal drift (10). Averaging across replicate samples, the power dissipated as heat was found to be $P_{diss} = 94 \pm 20$ nW. As the system is in steady state and not exchanging mass or work with the environment, the chemical energy converted by motor proteins must be dissipated as heat. However, there are multiple intermediate paths through which this energy can flow. A fraction of the energy from each ATP hydrolysis goes directly into heat, while another fraction goes into microtubule motion and propagates up in scale to drive the emergent large-scale flows before being converted to heat through viscous dissipation. We next asked what fraction of the total dissipated power propagates to the emergent large-scale flows.

From the mean flow speed and velocity correlation length, the power dissipated through viscous dissipation by the large-scale flows can be estimated as $P_{flow} \approx V_0 \mu \langle |\vec{v}(\vec{r},t)| \rangle^2_{\vec{r},t} / L^2$. Here, P_{flow} is the viscously dissipated power derived using dimensional analysis in the form of viscous dissipation of an incompressible fluid (15), $V_0 = 0.5$ μL is the system volume, and μ is the viscosity. Based on a previously published rheological characterization of microtubule active gels (16), we approximate the viscosity as a constant value, $\mu \cong 1$ mPa · s, leading to an estimate of $P_{flow} \approx 2 \times 10^{-7}$ nW. As the system is in steady state, the energy dissipated by these large-scale flows must be propagated from smaller length scales, and hence, P_{flow} provides an estimate of the energy propagated to these large length scales.

By comparing P_{diss}, the thermal dissipation rate, with P_{flow}, the power viscously dissipated by large-scale flows, we define the fraction of energy propagated to large-scale flows, $\eta = \frac{P_{flow}}{P_{diss}} \approx 2 \times 10^{-9}$. Hence, only a minute fraction of the chemical energy used by the system propagates into the emergent flows, demonstrating that the efficiency of this system for generating these flows is remarkably low (Fig. 1 *G*, *Inset*), far lower than the ~20% efficiency measured for individual kinesin (17) or for frog muscle where the peak efficiency can approach ~45% (18, 19). Thus, the large thermal dissipation must be due to either substantial energetic losses during the energy propagation across scales or a significant contribution to the thermal dissipation from chemical reactions other than ATP hydrolysis by K401.

We first tested whether the large thermal dissipation was due to a dominant contribution from the ATP regeneration system by measuring the dissipated power of a sample lacking both pyruvate kinase and phosphoenolpyruvate, the chemical fuel that drives the pyruvate kinase reaction. Averaging over the first measurement scan, the dissipated power was found to be $P_{diss,no\ reg} = 24.75 \pm 0.01$ nW (*SI Appendix*, Fig. S3), approximately one fourth of the value of the system containing the ATP regeneration system. While lower in samples lacking an ATP regeneration system, the dissipated power is still approximately nine orders of magnitude larger than $P_{flow} \approx 2 \times 10^{-7}$ nW, arguing that heat released by the ATP regeneration system cannot explain the small fraction of energy propagated to large length scales.

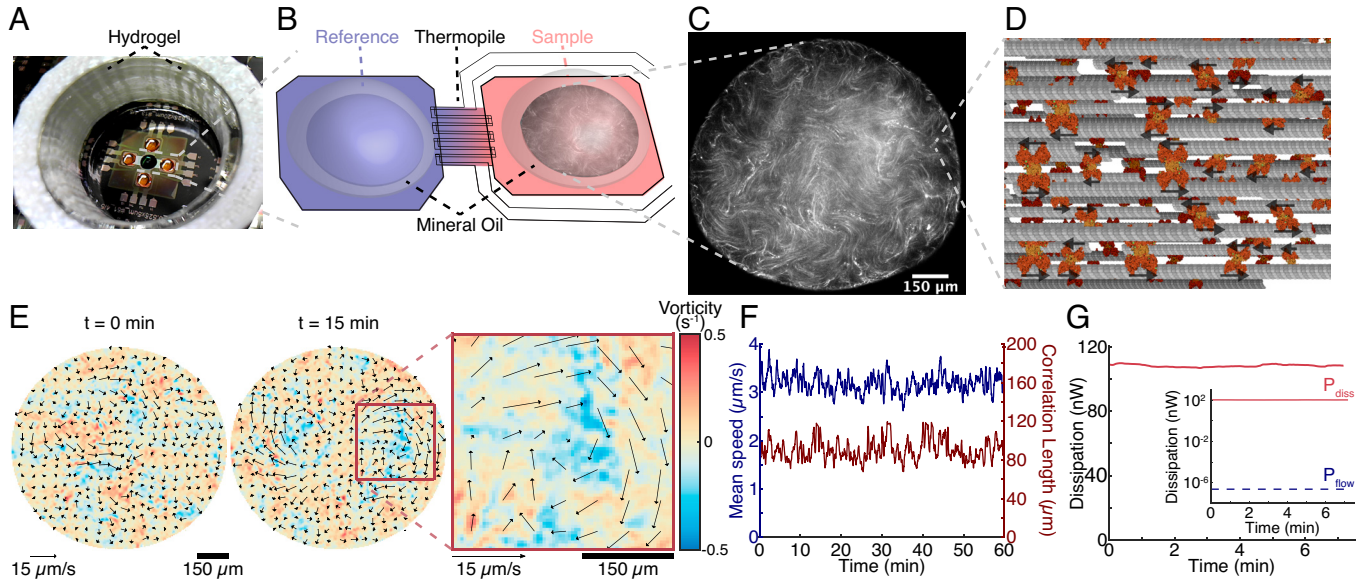

Fig. 1. Dynamics and heat dissipation of active microtubule networks. (*A*) Image of the calorimetry sensor. The green droplet is placed on the central reference pad, and the transparent droplets are placed on the exterior sample pads. To prevent evaporation, sample and reference droplets were covered with oil and sealed inside a hydrogel-lined enclosure. (*B*) Schematic of a sample reference pair. Differing heat production by the sample and reference leads to a temperature difference across the serpentine thermopile. (*C*) Droplet of an active microtubule gel of comparable size to those used in calorimetry. (*D*) Bundle of stabilized microtubules, whose extensile motion is driven by K401 motor clusters (*E*) Within droplets, microtubule active gels generate self-organized emergent flows. Color indicates local vorticity. Black arrows: velocity field. (*F*) Mean speed (blue) and correlation length (red) of the emergent flows reach a nonequilibrium steady state. (*G*) Thermal dissipation of an active gel measured using calorimetry. A sample lacking ATP was used as a reference. *Inset*: log plot showing measured thermal dissipation of the active gel, P_{diss} (red), and estimated viscous dissipation by large-scale flows, P_{flow} (blue). Data shown are for samples containing 1.5 mM ATP, 210 nM K401, and 16 μM tubulin.

Chemical Kinetics Model

To explore why the rate of energy use and hence the heat dissipation rate of these active gels is so large, we next developed a chemical kinetics model describing the reactions in our system (*SI Appendix*). In this model, the instantaneous heat dissipation is equal to the net change in enthalpy for each reaction times its respective reaction rate. Our model considers two reactions: ATP hydrolysis by kinesin and ATP regeneration by pyruvate kinase (Fig. 2*A* and *SI Appendix*). From these reactions, the thermal dissipation of the system is calculated as $\dot{Q} = V_{system} \times \left(\Delta H_{\mathrm{K401}} \times r_{K401} + \Delta H_{\mathrm{PK}} \times r_{PK}\right)$, where V_{system} is the system volume, ΔH_i is the volumetric enthalpy change for the reaction catalyzed by enzyme i, and r_i is the respective reaction rate. In this model, the reaction rate for the pyruvate kinase reaction follows Michaelis–Menten kinetics (20), while the K401 reaction rate incorporates the binding of K401 to microtubules in addition to the ATP binding by K401 (*SI Appendix*). Importantly, the model for the K401 reaction relies on the same assumptions as Michaelis–Menten kinetics, including that the system is well mixed and that the motors do not directly interact with each other. As the rate-limiting step for the overall reaction is ATP hydrolysis by kinesin, we further make the approximation that $r_{PK} \approx r_{K401}$ and hence $\dot{Q} \approx V_{system} \times \left(\Delta H_{K401} + \Delta H_{PK}\right) \times r_{kinesin}$ (*SI Appendix*).

Experimental Test of the Chemical Kinetics Model

To test the validity of this model, we repeated calorimetry measurements using samples with varying initial concentrations of ATP (Fig. 2*B*) or microtubules (Fig. 2*C*), holding the concentrations of all other components fixed. All model parameters were taken from the literature (*SI Appendix*, Table S1) except for a single fitting parameter, k_{cat}, which represents the maximum number of ATPs hydrolyzed per K401 per second. Simultaneously fitting the model to the ATP and microtubule titration series yielded close agreement with the measured data (Fig. 2 *A* and *B*). From our fit, we find $k_{cat} = 44.0 \pm 8.2\ \mathrm{s}^{-1}$ (mean ± 95% CI). As kinesins use one ATP per d = 8-nm step (21, 22), one can alternatively estimate k_{cat} from the unloaded motor speed, v, as $k_{cat} = \frac{v}{d}$. Measurements of the unloaded motor speed for various K401 constructs (12, 23–25) characterized using gliding assays fall within the range $v = 0.23 - 0.67\ \frac{\mu\mathrm{m}}{\mathrm{s}}$, implying a range of $k_{cat} = 29 - 84\ \mathrm{s}^{-1}$, consistent with the value of k_{cat} measured here. Intriguingly, this model does not consider the potential force dependence of the rate of ATP hydrolysis by K401 which may be present for large loads, and hence, these results are consistent with each microtubule-bound motor hydrolyzing ATP at its unloaded rate.

We next tested the model for varying concentrations of K401. The model assumes that the rate of each reaction is limited by enzyme concentration, and as the ATP hydrolysis reaction proceeds much slower than the ATP regeneration reaction, the concentration of K401 should limit the net reaction rate. Hence, the thermal dissipation is predicted to vary linearly with K401 concentration. To test this, we repeated calorimetry measurements titrating the concentration of K401 (Fig. 2*D*). While the thermal dissipation increases approximately linearly for low K401 concentrations, at higher K401 concentrations, the dissipation deviates from linearity and plateaus or perhaps even slightly decreases in contrast to model predictions. Thus, in this regime, one of the assumptions of the model must be violated. We hypothesize that at high K401 concentrations, the motors are distributed densely enough on microtubules that they begin to interact, potentially through mechanical coupling due to non-synchronous stepping (25).

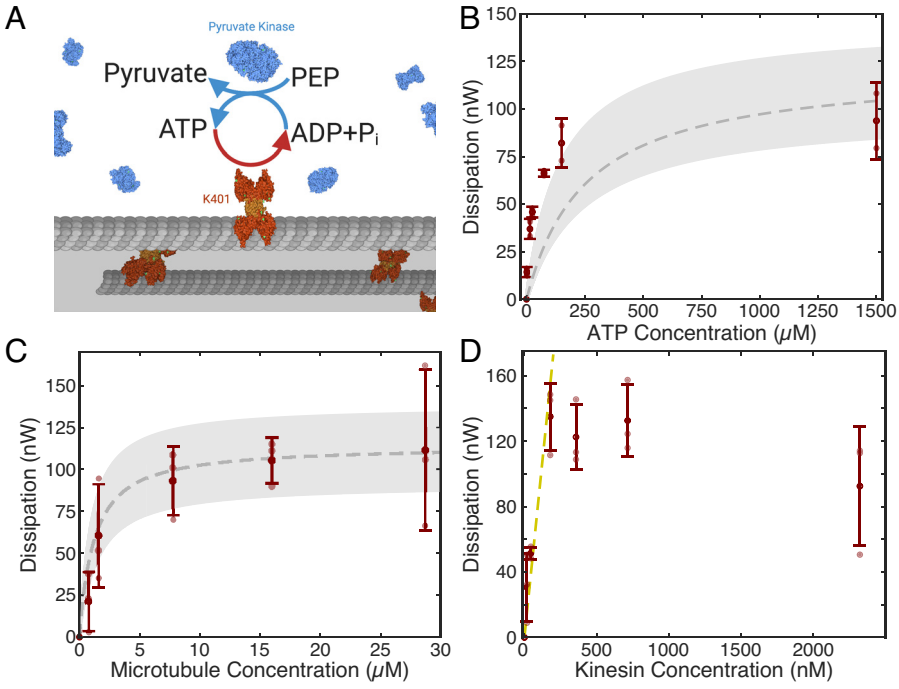

Fig. 2. Testing the chemical kinetics model. (*A*) System schematic showing the two chemical reactions included in the model: ATP hydrolysis by K401 and ATP regeneration by pyruvate kinase. (*B*) Thermal dissipation for samples prepared with varying initial ATP concentrations, 210 nM K401, and 16 μM tubulin. A sample lacking ATP was used as a reference. Data averaged over n = 2 independent replicates for each concentration. (*C*) Thermal dissipation for samples prepared with varying microtubule concentrations, 1.4 mM ATP, and 210 nM K401. A sample lacking microtubules was used as a reference (n = 3 independent replicates). (*D*) Thermal dissipation for samples prepared with varying kinesin concentrations, 1.4 mM ATP, and 16 μM tubulin. A sample lacking K401 was used as a reference (n = 3 independent replicates). Dark red points: measured dissipation ± propagated error (*Materials and Methods*). Light red points: mean dissipation for individual replicates. Dashed gray line: best fit for chemical kinetics model. Gray shade: Model predictions where k_{cat} and $K_{D,ATP}$ are varied across their fit values ± fitting error. Dashed gold line: Linear fit to data from the four lowest kinesin concentrations.

Large Thermal Dissipation Is Not from Singly Bound Motors

The chemical kinetics model assumes that all bound motors contribute to the dissipation, but the model cannot predict what fraction of this energy propagates to the scale of the emergent flows. At the protein scale, the small fraction of energy propagated to the emergent flow could be due to a large fraction of kinesin clusters that are bound to microtubules but do not cross-link them. Interfilament sliding requires that kinesin clusters simultaneously bind to and move along a pair of microtubules (Fig. 3*A*). However, a motor cluster can also be bound to a single microtubule. Such motor clusters would contribute to the overall heat production, but not to the emergent flows. To investigate this possibility, we made active gels where the chance of singly bound motors has been greatly reduced by permanently attaching motors to microtubules. This was accomplished by using a dimeric 560–amino acid truncation of human kinesin containing a C-terminal SNAP tag (SNAP-K560) which covalently binds with a benzyl guanine (BG) label incorporated into microtubules, effectively immobilizing one end of the motors (26) (Fig. 3*B* and *Materials and Methods*). As motor binding to microtubules via their head domain, but not the BG tag, strongly stimulates the ATPase activity of kinesins (23), essentially all ATP hydrolysis activities must be from SNAP-K560 cross-linking and sliding microtubules.

We first confirmed that SNAP-K560 samples formed active gels with similar properties to K401 samples (Fig. 3 *C* and *D*). Using PIV, we measured the mean speed and the flow velocity correlation length of samples containing 1.4 mM ATP to be $\langle|\vec{v}(\vec{r},t)|\rangle_{\vec{r},t}^{SNAP} = 0.45 \pm 0.18 \frac{\mu m}{s}$ and $L_{SNAP} = 188 \pm 20\ \mu m$ (Fig. 3 *E* and *F*). The velocity correlation length of the SNAP-K560 gel is slightly larger than that of K401 gels, the mean speed of the SNAP-K560 gel is slightly smaller, and microtubules appear to be more bundled, suggesting there may be small differences in how these motors organize microtubules and generate motion. As was done for K401 gels, we estimate the power dissipated through viscous dissipation by the large-scale flows to be $P_{flow,SNAP} \approx 3 \times 10^{-9}$ nW lower than the estimate of $P_{flow} \approx 2 \times 10^{-7}$ nW for K401 gels due to the decreased mean speed and increased flow velocity correlation length of SNAP-K560 gels. We next used calorimetry to measure the thermal dissipation rate of a SNAP-K560 gel to be $P_{diss,SNAP} = 62 \pm 18$ nW similar to but slightly smaller than the value measured for K401 gels (Fig. 3*G*) and far greater than $P_{flow,SNAP} \approx 3 \times 10^{-9}$ nW. Additional experiments show that the trend of lower speeds and similar but slightly lower thermal dissipation rates for SNAP-K450 gels holds for systems containing a range of different initial ATP concentrations (*SI Appendix*, Figs. S4 and S5), potentially due to SNAP-K450 gels containing a lower concentration of active motors. The observations that the thermal dissipation is similar for SNAP-K560 and K401 gels, the emergent flow properties differ only slightly, and in both cases, $P_{diss} \gg P_{flow}$ argue that the large thermal dissipation is not due to ATP hydrolysis by noncross-linking motors bound solely to individual microtubules.

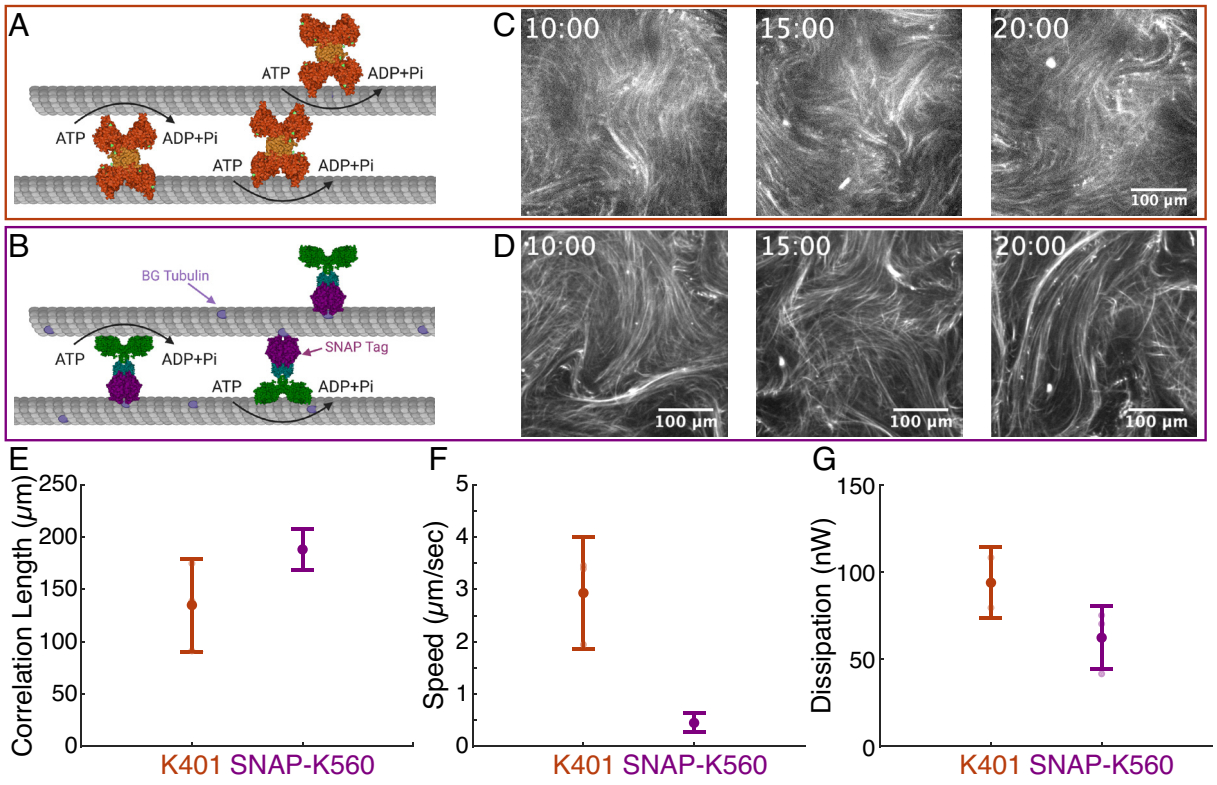

Fig. 3. Dissipation and efficiencies of SNAP-K560 gels. (*A*) K401 hydrolyzes ATP when bound to single microtubules or microtubule pairs. (*B*) The SNAP tag of K560 binds to the BG motif on tubulin incorporated into microtubules. SNAP-K560 only hydrolyzes ATP when cross-linking microtubules. (*C*) K401 activity drives microtubule gel dynamics (time in min:s). (*D*) SNAP-K560 organizes microtubules into dynamic active gels that are similar to K401 gels (time in min:s). Velocity–velocity correlation length (*E*) and average speed (*F*) measured using PIV for K401 (n = 3) and SNAP-K560 (n = 1) gels. (*G*) Measured dissipation for K401 (n = 2) and SNAP-K560 (n = 3) gels. For both K401 and SNAP-K560 measurements, a sample lacking ATP was used as a reference. Error bars in *E*–*G* represent propagated error (*SI Appendix*). Transparent points: average values for individual replicates. Data shown are for samples containing 1.4 mM ATP and 16 μM tubulin, and the K401 sample contains 210 nM K401.

Estimate of Energy Losses across Scales

While changing the initial concentrations of ATP, microtubules, and K401 results in differing thermal dissipations, mean speeds, and velocity correlation lengths (Fig. 2 and *SI Appendix*, Fig. S4) in all cases, the fraction of energy propagated to large length scales remains extremely low, ~10^{-8} to 10^{-9}, raising the question of why so little of the dissipated power propagates to large length scales. The energy from ATP hydrolysis at the scale of individual motors must propagate up across length scales, and inefficiencies could potentially arise at each step (Fig. 4). A back-of-the-envelope calculation can provide insight. At the scale of an individual motor, there is a tight coupling between ATP hydrolysis and translocation (21, 22). The maximum amount of work that can be extracted per ATP hydrolysis, W, is given by the product of the maximum force a motor can exert, F_{stall}, and the motor step size, d. Taking the stall force to be (27) $F_{stall} \approx 5$ pN and step size (28) $d = 8$ nm, one arrives at an estimate of $W_{max} \approx 40$ pN · nm. As sliding friction between microtubules has been shown to be weak and dominated by hydrodynamic interactions (29), we use a slender body approximation for the force per motor as the force required to move a microtubule along its long axis through water, given by $F \approx \frac{2\pi\mu l}{ln\left(\frac{l}{a}\right)}v$. Taking typical microtubule dimensions of length (14), $l = 1$ μm, and radius (30), $a = 12.5$ nm, the viscosity of water as $\mu \cong 1$ mPa · s, and an unloaded motor speed of $v \approx 0.3\frac{\mu m}{s}$ yields $F \approx 0.4$ fN or an energy per 8-nm step of $W \approx 3 \times 10^{-3}$ pN · nm. In this case, motors only extract a fraction of the energy available from ATP hydrolysis, given by $\gamma_{motor} = \frac{W}{W_{max}} \approx 8 \times 10^{-5}$. Hence, even at the scale of a single motor, large inefficiencies can emerge. Furthermore, the standard conditions considered here contain 16 μM tubulin which, taking an average microtubule length of 1 μm and noting that microtubules contain ≈1,625 heterodimers per micron (31), corresponds to a microtubule concentration of ≈10 nM. If ≈95% of motors at a concentration of ≈210 nM are bound at a given time, as estimated using the binding reactions for the chemical kinetics model, this implies there are on average ≈20 motors bound per microtubule. If all motors walk at their unloaded speeds, then microtubule pairs will move at the same speed as when only a single motor is present, but ≈ 20× the ATP will be hydrolyzed. Thus, at the scale of a microtubule pair, the fraction of energy extracted from each ATP molecule will be further reduced by a factor of 20, leading to $\gamma_{MT\ pair} \approx 4 \times 10^{-6}$. Microtubules in the system are organized into bundles whose motion drives the emergent flows. As these bundles are long and thin, the slender body theory suggests that the resulting fluid motion should have only a logarithmic dependence on the bundle aspect ratio and hence be approximately independent of the bundle diameter. Thus, increasing the bundle diameter should have a minimal impact on the resulting flows while increasing the rate of ATP consumption rate per bundle due to the increased number of microtubules in a cross-section. Taking a bundle diameter of 0.5 μm coarsely estimated from microscopy, and a close-packed microtubule spacing of 25 nm, we estimate that bundles have $\approx \frac{\pi(0.25\,\mu m)^2}{\pi(0.0125\,\mu m)^2} = 400$ microtubules in a cross-sectional area, further reducing the efficiency to $\gamma_{bundle} \approx 1 \times 10^{-8}$, which is similar to our experimental measurements. Interactions between bundles could lead to additional inefficiencies. Thus, these calculations suggest that the energetic inefficiency of this active material results from an accumulation of losses at all scales.

Discussion

Here, we have used picocalorimetry to measure the thermal dissipation of an active cytoskeletal material. By comparing this dissipation with a characterization of the emergent nonequilibrium flow, we find that only a minute fraction of the system's total energy dissipation, approximately one-billionth of the total, propagates to the scale of the emergent flows. We show that this discrepancy is not due to noncross-linking motors and develop a chemical kinetics model of the heat generated by these active gels. The chemical kinetics model's success in accounting for the changes in the thermal dissipation with ATP and microtubule concentrations argues that, under these conditions, the molecular motors operate independently and are unloaded. The model's failure at higher motor concentrations suggests that in this regime, additional effects influence the system's dissipation. We speculate that mechanical effects, such as interference due to nonsynchronous stepping (25), could play a role. Finally, we perform an estimate that rationalizes the inefficiency of this active cytoskeletal material for generating emergent fluid flows, which suggests that substantial energy losses occur at all scales: at the levels of individual molecular motors (due to the tight coupling between ATP hydrolysis and translocation), pairs of cross-linked microtubules (due to unproductive load sharing between molecular motors),

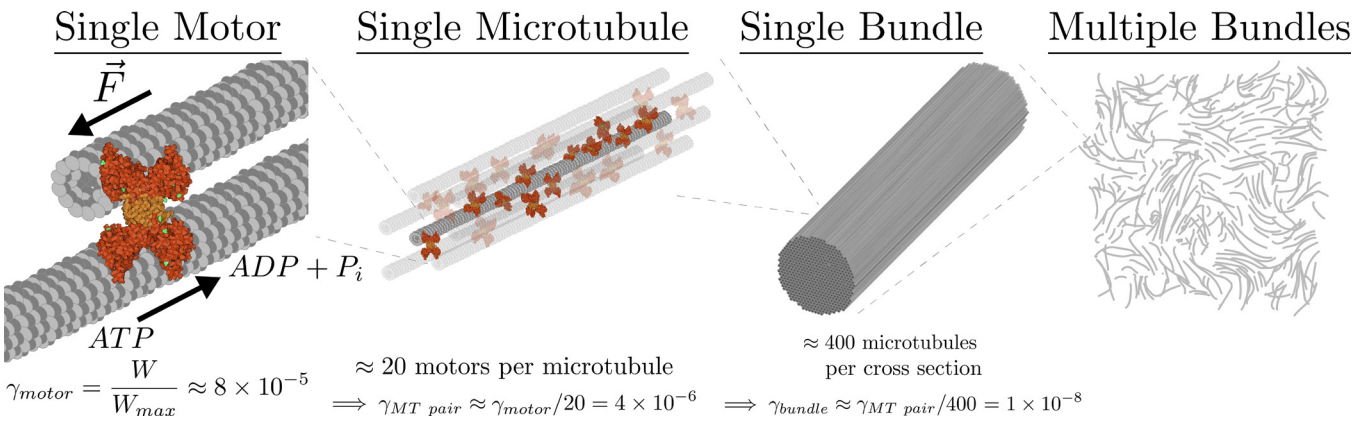

Fig. 4. Energy propagation across scales. Inefficiencies in the conversion of energy into motion happen at a number of scales. At the motor scale, moving a microtubule through water requires far less energy than is released through ATP hydrolysis. At the microtubule scale, many motors cross-linking a microtubule cause the microtubule to move at most at the speed of a single motor, but each motor hydrolyzes ATP. At the bundle scale, many microtubules are in a cross-section, but as the aspect ratio of bundles is large, fluid motion is approximately independent of bundle diameter. At the system scale, the interaction between multiple bundles could lead to further energetic losses.

and entire microtubule bundles (due to the large number of microtubules per bundle cross-section). Further inefficiencies could arise from uncoordinated stepping between motors (25), interactions between bundles, or other mechanisms (32).

Understanding the energy consumption of active materials is crucial for the engineering of practical materials. Recent work has considered the dissipation of nonequilibrium materials at different scales (32–35). At the microscale, irreversibility has been characterized through measuring the breaking of detailed balance for measured degrees of freedom (36–40), providing a lower bound on the entropy production rate. In a complementary approach, the Harada–Sasa relation (41) has been successfully applied to measure the dissipation of individual molecular motors (17, 42) or tracers in cells (43). While powerful, these approaches only provide a lower bound characterizing the observed degrees of freedom and are challenging to apply to the large-scale assemblies considered here. At the other extreme, recent theoretical work has considered dissipation in a continuum model of active nematics (44) and finds that energy is dissipated at the scale it is injected. As this model takes a continuum description of the material, dissipation at scales below the continuum limit is by necessity neglected. Rather than beginning with a continuum description, recent work by Yu et al. has considered the effects of coarse graining a discrete microscopic model on the entropy production rate, finding that the dissipation decreases with increasing coarse graining as a power law for certain classes of nonequilibrium networks (32). Similar to this model, our back-of-the-envelope calculation suggests that for the active gel considered here, the majority of the dissipation happens at length scales smaller than the continuum limit, with only $\approx 10^{-8}$ of the total energy used propagating beyond the scale of microtubule bundles, a number similar to the estimated dissipation loss in Yu et al. In the work presented here, by measuring the thermal dissipation, the total rate of energy consumption can be quantified, and this thermal dissipation can be compared with the estimated energy dissipation by flows on the largest length scales. Between these scales, whether or not the dissipation decreases as a power law remains to be tested.

Realizing the future potential of active biomimetic materials for producing mechanical work in complex engineered systems will require understanding and overcoming limitations in energetic efficiency. Addressing this challenge may require the design of such materials at the microscale, created from fundamental units whose architecture maximizes the amount of energy extractable as useful work. Eukaryotic cells use active cytoskeletal assemblies to perform the mechanical work that underlies diverse cellular functions ranging from cell motility to chromosome segregation (30). Much like the active gels considered here, these biological machines contain large numbers of motor proteins cross-linking cytoskeletal filaments, raising the question about their energetic efficiency at performing mechanical work. Understanding the energetic costs, constraints, and efficiencies of cytoskeletal structures in vivo (45) could inspire strategies for increasing the energetic efficiency of active biomimetic materials in vitro.

Materials and Methods

Protein Purification and Sample Composition. We prepared active gel samples as previously described (46). Briefly, 80 μM tubulin was polymerized into stable microtubules using the nonhydrolyzable GTP analog GMPCPP (Jena Biosciences NU-405) in a water bath at 37 °C for thirty minutes. Tubulin was 6% labeled with Alexa Fluor 647 NHS Ester (Invitrogen A-20006). All microtubules were prepared in one batch, flash-frozen, and thawed before use. Kinesin-1 streptavidin clusters were created by combining streptavidin (Invitrogen S-888) with an engineered *Drosophila* kinesin-1 truncated to the first 401 amino acids of the N-terminal and linked to an 87–amino acid C-terminal of a biotin tag with a monomer molecular weight taken to be 56 kDa (46). We expressed and purified the engineered kinesin from *Escherichia coli* and flash-froze the kinesin–streptavidin complexes after dimerization. We prepared a buffer solution consisting of 1% 35-kDa polyethylene glycol, "M2B" (80 mM PIPES, 2 mM $MgCl_2$, and 1 mM ethylene glycol tetraacetic acid (EGTA) in water adjusted to a pH of 6.8 with KOH), and oxygen scavengers and an ATP regeneration system consisting of DTT (ACROS Organics 16568), glucose (Sigma G7528), catalase (Sigma C40), glucose oxidase (Sigma G2133), ATP (Sigma A2383), DTT (ACROS Organics 16568), PEP (phosphoenolpyruvate, Alfa Aesar B20358), and pyruvate kinase/lactic dehydrogenase (PK/LDH, Sigma P-0294). This solution was also flash-frozen. To perform experiments, we thawed kinesin, polymerized microtubules, ATP aliquots, and our buffer solution, and mixed them in the correct proportions.

We prepared active gel samples with SNAP-K560 and BG microtubules as previously described by Chandrakar et al. (26). BG-labeled tubulin was made by labeling tubulin using BG-GLA-NHS (NEB S9151S) using a protocol by A. Hyman et al. (47). To create BG microtubules, 44 μM tubulin containing 6% BG-labeled tubulin was polymerized using GMPCPP at 37 °C. These BG microtubules are incubated with SNAP-K560 and 1 mM DTT in phosphate-buffered saline at room temperature for 30 min. To remove the SNAP-K560 attached to microtubules by the non-BG end, the SNAP-K560 and BG-microtubule mixture was first centrifuged at 21,000 RCF (Eppendorf Centrifuge 5424 R) for 10 min. Next, the pellet was dissolved in a high-salt dissociation buffer (pH 7.7) consisting of 350 mM NaCl, 1 mM $MgCl_2$, 1 mM ethylene glycol tetraacetic acid (EGTA), and 10 mM 4-(2-hydroxyethyl)-1-piperazineethanesulfonic acid. Afterward, it was left to incubate for 2 min at room temperature. The dissociation buffer was exchanged with M2B by again centrifuging at 21,000 RCF and then dissolving the pellet in M2B. The result is SNAP-K560-labeled microtubules which were added to the active sample described above before flash-freezing in liquid nitrogen.

Calorimetry Measurements and Analysis. We performed all calorimetry measurements using a recently developed micromachined picocalorimetry sensor (10). The sensor was calibrated using an internal heating element as previously described (10) (*SI Appendix*, Fig. S6). The thermal dissipation of active samples was measured as a function of ATP, microtubules, and kinesin concentrations. To evaluate the effect of the ATP concentration, four samples with a volume of 0.5 μL, each corresponding to a different concentration of ATP, were placed on the sample pads of the sensor, and a 0.5 μL sample without ATP was used as a reference. This procedure was repeated as necessary to obtain data for additional ATP concentrations and to replicate the measurements. The effects of the microtubule and kinesin concentrations were evaluated using the same method. Pipetting volumes of this size presents a challenge. To minimize errors associated with pipetting, a pipettor designed for low volumes was used (VWR catalog #89079-960) along with low retention pipette tips (VWR catalog #89368-978). While minimized to the extent possible, we believe pipetting error to be the dominant error source in these measurements. All sample and reference droplets were covered with 1.5 μL mineral oil and sealed inside the hydrogel-lined enclosure to minimize evaporation during the measurements. One limitation of this system is the requirement of a thermal stabilization time once samples have been placed on the sensor, which precludes measurement of rapid heat exchange upon sample mixing. After loading the samples, the measurement system was allowed to stabilize for a period of 20 min before commencing the measurements. The sample of interest was selected using a rotary switch, and the voltage signal of the corresponding thermopile was measured with a Keithley 2182A Nanovoltmeter. Each sample was measured for a period of 7.17 min before moving on to the next sample. The samples were measured in a random sequence to eliminate any systematic errors. Since the microscopy observations of the velocity of the active gels were obtained for approximately one hour, all calorimetry scans were initiated within one hour from activating the samples.

Confocal Microscopy and PIV Data Analysis. We performed microscopy with a 10× objective on an Olympus DSU Spinning Disk and a Yokogawa CSU-X1 Spinning Disk with a Nikon TE2000 base, both attached to a Hamamatsu ImagEM CCD camera (C9100-13). We managed the microscope equipment using μManager software (48).

We calculated flow fields from the microscopy data using the MATLAB PIVlab plugin (49). In processing the data, we generated masks when necessary to crop out material at the oil–water interface. We used the PIV algorithm at the level

of four passes, with windows of 128, 32, 16, and 8 pixels. Additional settings included deforming these windows using spline deformation and removing all preprocessing techniques such as CLAHE.

We calculate the mean speed $\langle |\vec{v}(\vec{r},t)| \rangle_{\vec{r},t}$ from the velocity field as

$$\left\langle \left| \vec{v}\left(\vec{r},t\right) \right| \right\rangle_{\vec{r},t} = \frac{1}{T}\sum_{t}^{T} \left\langle \left| \vec{v}\left(\vec{r},t\right) \right| \right\rangle_{\vec{r}}$$

where T is the number of frames evaluated. Additionally, for each frame, t, we calculate the velocity autocorrelation, $A_{vel}(r,t)$, as

$$A_{vel}(r,t) = \left\langle \frac{\langle v(r,t)\cdot v(r',t)\rangle}{\langle v(r',t)\cdot v(r',t)\rangle} \right\rangle = \frac{2}{N(N-1)}\sum_{j}^{N}\sum_{j<i}^{N}\frac{v\left(r_i,t\right)\cdot v\left(r_j,t\right)}{v\left(r_i,t\right)\cdot v\left(r_i,t\right)}.$$

This correlation is evaluated in Fourier space to reduce computation time. For each time point, τ, values of the velocity autocorrelation, $A_{vel}(r,\tau)$, were fit to an exponential of the form $A_{vel}(r,\tau) = Ae^{-\frac{t}{B}} + C$ for values of r ranging from 5 PIV bins ($\cong$ 25 μm) to the value of r such that $A_{vel}(r,\tau) = 0$. From this exponential fit, the correlation length, or decay length, is taken as $\lambda(\tau) = -B \times \log\left(\frac{0.3-C}{A}\right)$ and temporal averages, $\langle\lambda(\tau)\rangle_{\tau}$, are reported as the flow correlation length for the experiment. Example plots of the average velocity autocorrelation and an example time point with exponential fit are given in *SI Appendix*, Fig. S1.

Error Analysis. For calorimetry and PIV measurements, the reported error takes into account both the within-experiment variance, $\sigma^2_{measurement}$, and the variance between replicates, $\sigma^2_{replicates}$. The within-experiment variance was calculated as

$$\sigma^2_{measurement} = \frac{1}{N_{replicates}}\sum_{i=1}^{N_{replicates}}\sigma_i^2, \qquad [1]$$

where $N_{replicates}$ is the total number of replicates for the given condition, and σ_i^2 is the within-experiment variance for replicate i. For conditions with multiple replicates, the variance between replicates was calculated as the variance between replicate means.

$$\sigma^2_{replicates} = \left(\frac{1}{N_{replicates}-1}\sum_{i=1}^{N_{replicates}}\left(\mu_i - \langle\mu\rangle\right)^2\right), \qquad [2]$$

where μ_i is the mean value for replicate i, and $\langle\mu\rangle$ is given by

$$\langle\mu\rangle = \frac{1}{N_{replicates}}\sum_{i=1}^{N_{replicates}}\mu_i. \qquad [3]$$

From these, the net error for the condition, referred to in the main text as the propagated error, was calculated as

$$\sigma = \sqrt{\sigma^2_{measurement} + \sigma^2_{replicates}}. \qquad [4]$$

Unless otherwise stated, values reported in the paper are given as $\langle\mu\rangle \pm \sigma$.

Figure Illustrations. Cartoons in Figs. 1*D*, 2*A*, and 3 *A* and *B* were created with BioRender.com. K401, SNAP-K560, and pyruvate kinase cartoons were created using Illustrate (50).

Data, Materials, and Software Availability. Custom MATLAB code for analyzing the PIV data is available at https://github.com/bezlemma/PIVanalysis. All other data are included in the manuscript and/or *SI Appendix*. Microscopy images are available from the corresponding authors upon reasonable request. Plasmids for K401 and SNAP-K560 are available from Zvonimir Dogic upon request.

ACKNOWLEDGMENTS. This project was supported by the Harvard University Materials Research Science and Engineering Center (MRSEC), which is funded by the NSF under grants DMR-1420570 and DMR-2011754 and by NSF DMR-2004380 (to D.J.N.). This work was performed in part at the Harvard University Center for Nanoscale Systems (CNS), a member of the National Nanotechnology Coordinated Infrastructure Network (NNCI), which is supported by the NSF under NSF award no. ECCS-2025158. We acknowledge support from Brandeis NSF MRSEC, BioInspired Soft Materials, DMR-2011846. Z.D. acknowledges support of NSF-DMR-2004617. D.J.N. acknowledges discussions with participants of the "Active 20" and "Cellular Energetics" KITP programs, supported in part by the NSF under grant no. NSF PHY-1748958, NIH grant no. R25GM067110, and the Gordon and Betty Moore Foundation grant no. 2919.02. J.B. acknowledges support from the NSF through the UC San Diego Materials Research Science and Engineering Center (UCSD MRSEC), DMR-2011924. P.J.F. acknowledges the Gordon and Betty Moore Foundation for support as a Physics of Living Systems Fellow through grant no. GBMF4513.

Author affiliations: [a]Physics of Living Systems, Department of Physics, Massachusetts Institute of Technology, Cambridge, MA 02139; [b]Department of Physics, Brandeis University, Waltham, MA 02454; [c]John A. Paulson School of Engineering and Applied Sciences, Harvard University, Cambridge, MA 02138; [d]Department of NanoEngineering, University of California San Diego, La Jolla, CA 92093; [e]Department of Physics, Harvard University, Cambridge, MA 02138; [f]Department of Physics, University of California, Santa Barbara, CA 93106; [g]Department of Molecular and Cellular Biology, Harvard University, Cambridge, MA 02138; and [h]Center for Computational Biology, Flatiron Institute, New York, NY 10010

Author contributions: P.J.F., J.B, D.J.N, and J.J.V. designed research; P.J.F., J.B., B.L., J.Z., and W.I. performed research; P.C., R.B., and Z.D. contributed new reagents/analytic tools; P.J.F., J.B., B.L., J.Z., and W.I. analyzed data; and P.J.F., J.B., B.L., D.J.N, and J.J.V. wrote the paper.

1. R. Zhang *et al.*, Spatiotemporal control of liquid crystal structure and dynamics through activity patterning. *Nat. Mater.* **20**, 875–882 (2021).
2. G. Duclos *et al.*, Topological structure and dynamics of three-dimensional active nematics. *Science* **367**, 1120–1124 (2020).
3. P. J. Foster, S. Fürthauer, M. J. Shelley, D. J. Needleman, Active contraction of microtubule networks. *Elife* **4**, e10837 (2015).
4. S. Fürthauer *et al.*, Self-straining of actively crosslinked microtubule networks. *Nat. Phys.* **15**, 1295–1300 (2019).
5. P. J. Foster, S. Fürthauer, M. J. Shelley, D. J. Needleman, From cytoskeletal assemblies to living materials. *Curr. Opin. Cell Biol.* **56**, 109–114 (2019).
6. K.-T. Wu *et al.*, Transition from turbulent to coherent flows in confined three-dimensional active fluids. *Science* **355**, eaal1979 (2017).
7. T. Sanchez, D. T. N. Chen, S. J. DeCamp, M. Heymann, Z. Dogic, Spontaneous motion in hierarchically assembled active matter. *Nature* **491**, 431–434 (2012).
8. D. Needleman, Z. Dogic, Active matter at the interface between materials science and cell biology. *Nat. Rev. Mater.* **2**, 17048 (2017).
9. M. C. Marchetti *et al.*, Hydrodynamics of soft active matter. *Rev. Mod. Phys.* **85**, 1143–1189 (2013).
10. J. Bae *et al.*, A micromachined picocalorimeter sensor for liquid samples with application to chemical reactions and biochemistry. *Adv. Sci.* **8**, 2003415 (2021).
11. D. D. Pollock, *Thermoelectricity: Theory, Thermometry, Tool* (American Society for Testing Materials, 1985).
12. T. E. Bate, E. J. Jarvis, M. E. Varney, K.-T. Wu, Collective dynamics of microtubule-based 3D active fluids from single microtubules. *Soft Matter* **15**, 5006–5016 (2019).
13. G. Henkin, S. J. DeCamp, D. T. N. Chen, T. Sanchez, Z. Dogic, Tunable dynamics of microtubule-based active isotropic gels. *Philos. Trans. A Math. Phys. Eng. Sci.* **372**, 20140142–20140142 (2014).
14. S. J. DeCamp, G. S. Redner, A. Baskaran, M. F. Hagan, Z. Dogic, Orientational order of motile defects in active nematics. *Nat. Mater.* **14**, 1110–1115 (2015).
15. T. E. Faber, *Fluid Dynamics for Physicists* (Cambridge University Press, 1995).
16. D. A. Gagnon *et al.*, Shear-induced gelation of self-yielding active networks. *Phys. Rev. Lett.* **125**, 178003 (2020).
17. T. Ariga, M. Tomishige, D. Mizuno, Nonequilibrium energetics of molecular motor kinesin. *Phys. Rev. Lett.* **121**, 218101 (2018).
18. A. V. Hill, The mechanical efficiency of frog's muscle. *Proc. Biol. Sci.* **127**, 434–451 (1939).
19. C. J. Barclay, Energetics of contraction. *Compr. Physiol.* **5**, 961–995 (2015).
20. J. Oria-Hernández, N. Cabrera, R. Pérez-Montfort, L. Ramírez-Silva, Pyruvate kinase revisited. *J. Biol. Chem.* **280**, 37924–37929 (2005).
21. M. J. Schnitzer, S. M. Block, Kinesin hydrolyses one ATP per 8-nm step. *Nature* **388**, 386–390 (1997).
22. D. L. Coy, M. Wagenbach, J. Howard, Kinesin takes one 8-nm Step for each ATP that it hydrolyzes. *J. Biol. Chem.* **274**, 3667–3671 (1999).
23. K. M. Brendza, D. J. Rose, S. P. Gilbert, W. M. Saxton, Lethal kinesin mutations reveal amino acids important for ATPase activation and structural coupling. *J. Biol. Chem.* **274**, 31506–31514 (1999).
24. T. D. Ross *et al.*, Controlling organization and forces in active matter through optically defined boundaries. *Nature* **572**, 224–229 (2019).

25. P. Bieling, I. A. Telley, J. Piehler, T. Surrey, Processive kinesins require loose mechanical coupling for efficient collective motility. *EMBO Rep.* **9**, 1121–1127 (2008).
26. P. Chandrakar *et al.*, Engineering stability, longevity, and miscibility of microtubule-based active fluids. *Soft Matter* **18**, 1825–1835 (2022).
27. A. S. Khalil *et al.*, Kinesin's cover-neck bundle folds forward to generate force. *Proc. Natl. Acad. Sci. U.S.A.* **105**, 19247–19252 (2008).
28. K. Svoboda, C. F. Schmidt, B. J. Schnapp, S. M. Block, Direct observation of kinesin stepping by optical trapping interferometry. *Nature* **365**, 721–727 (1993).
29. A. Ward *et al.*, Solid friction between soft filaments. *Nat. Mater.* **14**, 583–588 (2015).
30. B. Alberts *et al.*, *Molecular Biology of the Cell* (Garland Science, 2007).
31. C. M. Waterman-Storer, E. D. Salmon, How microtubules get fluorescent speckles. *Biophys. J.* **75**, 2059–2069 (1998).
32. Q. Yu, D. Zhang, Y. Tu, Inverse power law scaling of energy dissipation rate in nonequilibrium reaction networks. *Phys. Rev. Lett.* **126**, 080601 (2021).
33. É. Fodor, M. E. Cates, Active engines: Thermodynamics moves forward. *EPL* **134**, 10003 (2021).
34. T. Markovich, É. Fodor, E. Tjhung, M. E. Cates, Thermodynamics of active field theories: Energetic cost of coupling to reservoirs. *Phys. Rev. X.* **11**, 021057 (2021).
35. L. Tociu, G. Rassolov, É. Fodor, S. Vaikuntanathan, Inferring dissipation from static structure in active matter. arXiv (2020). https://doi.org/10.48550/arXiv.2012.10441 (accessed 22 July 2021).
36. C. Battle *et al.*, Broken detailed balance at mesoscopic scales in active biological systems. *Science* **352**, 604–607 (2016).
37. T. H. Tan *et al.*, Scale-dependent irreversibility in living matter. arXiv [physics.bio-ph] (2021). https://doi.org/10.48550/arXiv.2107.05701 (Accessed 3 August 2021).
38. J. Li, J. M. Horowitz, T. R. Gingrich, N. Fakhri, Quantifying dissipation using fluctuating currents. *Nat. Commun.* **10**, (2019).
39. D. S. Seara *et al.*, Entropy production rate is maximized in non-contractile actomyosin. *Nat. Commun.* **9**, 4948 (2018).
40. J. Gladrow, N. Fakhri, F. C. MacKintosh, C. F. Schmidt, C. P. Broedersz, Broken detailed balance of filament dynamics in active networks. *Phys. Rev. Lett.* **116**, 248301 (2016).
41. T. Harada, S.-I. Sasa, Equality connecting energy dissipation with a violation of the fluctuation-response relation. *Phys. Rev. Lett.* **95**, 130602–130604 (2005).
42. S. Toyabe *et al.*, Nonequilibrium energetics of a single F1-ATPase molecule. *Phys. Rev. Lett.* **104**, 198103 (2010).
43. É. Fodor *et al.*, Nonequilibrium dissipation in living oocytes. *EPL* **116**, 30008 (2016).
44. R. Alert, J.-F. Joanny, J. Casademunt, Universal scaling of active nematic turbulence. *Nat. Phys.* **16**, 682–688 (2020).
45. X. Yang *et al.*, Physical bioenergetics: Energy fluxes, budgets, and constraints in cells. *Proc. Natl. Acad. Sci. U.S.A.* **118**, e2026786118 (2021).
46. A. M. Tayar, L. M. Lemma, Z. Dogic, Assembling microtubule-based active matter. *Methods Mol. Biol.* **2430**, 151–183 (2022).
47. A. Hyman *et al.*, Preparation of modified tubulins. *Methods Enzymol.* **196**, 478–485 (1991).
48. A. D. Edelstein *et al.*, Advanced methods of microscope control using μManager software. *J. Biol. Methods* **1**, e10 (2014).
49. W. Thielicke, E. Stamhuis, PIVlab – Towards User-friendly, Affordable and Accurate Digital Particle Image Velocimetry in MATLAB. *J. Open Res. Software* **2** (2014).
50. D. S. Goodsell, L. Autin, A. J. Olson, Illustrate: Software for biomolecular illustration. *Structure/Folding and Design* **27**, 1716–1720.e1 (2019).